

# Turbulence structure and similarity in the separated flow above a low building in the atmospheric boundary layer

Akon, A.F.; Kopp, Gregory

DOI:

[10.1016/j.jweia.2018.09.016](https://doi.org/10.1016/j.jweia.2018.09.016)

License:

Creative Commons: Attribution-NonCommercial-NoDerivs (CC BY-NC-ND)

*Document Version*

Peer reviewed version

*Citation for published version (Harvard):*

Akon, AF & Kopp, G 2018, 'Turbulence structure and similarity in the separated flow above a low building in the atmospheric boundary layer', *Journal of Wind Engineering and Industrial Aerodynamics*, vol. 182, pp. 87-100. <https://doi.org/10.1016/j.jweia.2018.09.016>

[Link to publication on Research at Birmingham portal](#)

## General rights

Unless a licence is specified above, all rights (including copyright and moral rights) in this document are retained by the authors and/or the copyright holders. The express permission of the copyright holder must be obtained for any use of this material other than for purposes permitted by law.

- Users may freely distribute the URL that is used to identify this publication.
- Users may download and/or print one copy of the publication from the University of Birmingham research portal for the purpose of private study or non-commercial research.
- User may use extracts from the document in line with the concept of 'fair dealing' under the Copyright, Designs and Patents Act 1988 (?)
- Users may not further distribute the material nor use it for the purposes of commercial gain.

Where a licence is displayed above, please note the terms and conditions of the licence govern your use of this document.

When citing, please reference the published version.

## Take down policy

While the University of Birmingham exercises care and attention in making items available there are rare occasions when an item has been uploaded in error or has been deemed to be commercially or otherwise sensitive.

If you believe that this is the case for this document, please contact [UBIRA@lists.bham.ac.uk](mailto:UBIRA@lists.bham.ac.uk) providing details and we will remove access to the work immediately and investigate.

# **Turbulence structure and similarity in the separated flow above a low building in the atmospheric boundary layer**

Abul Fahad Akon & Gregory A. Kopp\*  
Boundary Layer Wind Tunnel Laboratory, Faculty of Engineering  
University of Western Ontario, London, ON, Canada

## **Abstract**

Separated and reattaching flows over sharp-leading-edge bluff bodies are important to investigate in order to improve our understanding of practical flows such as the case of low-rise buildings in the atmospheric boundary layer. In this study, Particle Image Velocimetry measurements of the separated-reattaching flows over the roof surface of a low-rise building model were taken for six different turbulent boundary layer conditions. The results were analyzed to understand how the incident turbulence affects the flow field of the separation bubbles above the low-rise building roof. The mean flow field above the roof-surface was found to be approximately similar across the six terrain conditions using the mean reattachment length in the streamwise direction and the maximum mean thickness of the separated shear layer in the vertical direction. However, the turbulence stresses are not similar which is attributed to high levels of initial turbulence kinetic energy in the separated shear layer. This leads to fundamental differences in the initial development of the separated flow when compared to flows with lower turbulence in the incident stream. The results indicate that the Kelvin-Helmholtz instability may be altered, or perhaps even suppressed, in the initial flow development region. This leads to substantially different turbulence statistics and characteristics within the separated shear layers.

## **Keywords**

Building aerodynamics; separated flows; reattaching flows; low-rise buildings; turbulence structure; atmospheric boundary layers.

---

\* Corresponding Author; [gakopp@uwo.ca](mailto:gakopp@uwo.ca)

# 1 Introduction

Flows over sharp-edged bluff bodies have received special attention by researchers because of their numerous practical applications including atmospheric boundary layer flows around buildings and bridges. Of fundamental importance to the aerodynamic loading is the character of the separated shear layer (SSL). There have been numerous studies on the details of the development and loading effects of SSLs in uniform smooth flow. Kiya & Sasaki (1983, 1985) investigated the flow downstream of the separation at the upper edge of a two-dimensional blunt flat plate placed in uniform upstream flow with low levels of free-stream turbulence. Their investigations revealed the presence of Kelvin-Helmholtz (K-H) vortices in the separated flow region near the leading edge much like those in a classical mixing layer (see, e.g., Brown & Roshko, 1974). Downstream of the leading edge, these Kelvin-Helmholtz vortices increase in size due to pairing and, eventually breaking down into turbulence. Near the mean reattachment point, the largest surface pressure fluctuations occur due to this turbulence. These authors also observed the shedding of large-scale vortices from the separation bubble, which are associated with fluctuations of the reattachment length and flapping motions of the SSL. However, closer to the separation point, the surface pressure fluctuations, although relatively small, are related to the transient nature of the K-H instability.

For wind loads, the effects of atmospheric turbulence is critical. Emphasizing the importance of the SSL, Gartshore (1973) was the first to show that small-scale turbulence on the stagnation streamline was sufficient to produce the effects attributed to turbulence on the flow around the bluff body. Recently, Lander *et al.* (2016), repeating many aspects of Gartshore's experiments, showed that this small-scale turbulence causes a by-pass transition such that the normal development of turbulence in the SSL occurs much earlier, closer to the leading edge.

Saathoff & Melbourne (1997) investigated many of the effects of upstream turbulence properties on the flow field around a two-dimensional rectangular cylinder for a range of turbulence intensity and

length scales. Their investigation revealed that the free-stream turbulence interacts with the separated shear layer in a variety of ways. For example, higher levels of free-stream turbulence cause greater perturbations to the separated shear layer and cause the vortices to roll-up closer to the leading edge, as confirmed by the detailed flow measurements in Lander *et al.* (2016). This leads to three effects. When the free-stream turbulence level is larger, (i) there is a reduction in the mean reattachment length, (ii) there are larger surface pressure fluctuations, (iii) which occur relatively closer to the leading edge, i.e., at a smaller  $x/X_r$  location, where  $X_r$  is the mean reattachment length. Of significance, Saathoff & Melbourne (1997) also observed that there are larger magnitude surface pressure fluctuations when there are larger integral length scales in the free-stream turbulence. However, the location of maximum surface pressure fluctuations was not observed to be affected by the integral scales over the range they studied. These authors speculate that for cases with smaller integral scales, the gusts “carry away” the vortices in the shear layer more frequently, not allowing them to grow in strength. In contrast, for turbulence with large integral scales, the gusts are relatively less frequent and allow more time for the shear layer vortices to grow in strength, which causes the surface pressures to fluctuate at a higher level. These effects on surface pressures have also been observed in the regions of separated flow on the roofs of low-rise buildings in the atmospheric boundary layer (e.g., see Fernandez-Caban & Masters, 2018, for a recent example). However, a complete understanding of how different levels of turbulence intensities and length scales in the incident flow affect the mean and fluctuating flow fields in and around the separation bubble has not been developed.

While there have been many studies examining wind loads, there have been only a limited number of studies investigating the separated and reattaching flow fields around sharp-edged, three-dimensional, surface-mounted bluff bodies (i.e., buildings) in turbulent boundary layer conditions. Castro and Robins (1977) show that for surface-mounted cubes, there is intermittent reattachment on the upper surface and that the Reynolds stress components play an important role in characterizing the aerodynamic loading.

Although these results also suggest that the decay of the wake is a strong function of the upstream turbulence, velocity field measurements for a wide range of turbulence intensities and length scales have not been conducted. Hence, the nature of the mean and turbulent flow field of the roof separation bubble, and their dependence on the upstream turbulence properties, are not clearly understood.

Kim *et al.* (2003) took detailed velocity field measurements around a low-rise building placed in a turbulent boundary layer. Their data reveal that a short distance along the separated shear layer, turbulent kinetic energy attains its maximum value and then gradually reduces downstream. Essel *et al.* (2015) observe the presence of negative Reynolds shear stress and regions of negative production near the separation point on a forward-facing step. However, how the magnitudes of Reynolds stresses and the production of turbulence vary with the upstream turbulence characteristics for a low-rise building, and how these quantities affect the aerodynamics, have not been studied in detail.

Finally, there is also little available information on the scaling parameters which control or normalize the SSL and, more generally, the separated-reattaching flow at bluff-body edges. For low-rise buildings in the atmospheric boundary layer (ABL), Lin *et al.* (1995) argued that the distance from the wall stagnation point to the roof edge (i.e., the separation point),  $H_s$ , was the critical geometric scale. These authors then suggested that building height,  $H$ , could be a proxy for  $H_s$ . Akon & Kopp (2016) found that, for a single building shape in six distinct terrain conditions,  $H_s$  was a fixed proportion of  $H$ , making this a useful geometric parameter. The other obvious scaling parameters are related to the flow field, such as the distance from the separation point to the mean reattachment point,  $X_r$ , or the maximum value of the mean thickness of the separation bubble,  $T_b$ . For buildings, Akon & Kopp (2016) showed that  $X_r$  depends strongly on turbulence intensity,  $I_u$ , but approaches an asymptotic limit for relatively high values of  $I_u$ . Castro & Haque (1988), in their examination of a SSL in smooth flow used  $T_b$ , but it is not clear how this parameter varies with the stream turbulence characteristics or body geometry since it has not been systematically investigated.

The objective of this paper is to examine the flow similarity in the separated-reattaching flow on the upper surface of a low-rise building, as a function of the approaching ABL conditions. In particular, the roles of possible scaling parameters are examined using Time-Resolved Particle Image Velocimetry measurements in six distinct terrain conditions. The mean and fluctuating velocity fields in and around the roof separation bubbles are examined in detail in order to meet this objective.

## 2 Experimental details

A 1/50 scaled model of Texas Tech University (TTU) Wind Engineering Research Field Laboratory (WERFL) Building (Levitan & Mehta, 1992) was used in these experiments. This building geometry was chosen because it has been widely studied and has aspect ratios common to many low-rise buildings. The model building has plan dimensions of length,  $L$ , by width,  $W$ , of 18.3 cm  $\times$  27.5 cm, and roof height,  $H = 7.8$  cm. Thus, the wall aspect ratios were  $L/H = 2.35$  and  $W/H = 3.53$ . The roof-height mean wind speed was 6.7 m/s, yielding a Reynolds number of 35,000. A single wind direction is used in this study, which is perpendicular to the wide face of the building. The blockage ratio for this configuration is 0.3%.

A schematic of the coordinate system and set-up is shown in Figure 1. A Cartesian coordinate system is used in the current analysis such that streamwise and vertical directions are labelled as the  $x$  and  $y$  axes, respectively. The midplane of the windward wall at the roof edge considered to be the origin,  $(x,y) = (0,0)$ , which is convenient for describing the flow above the roof. For the velocity profiles describing the upstream boundary layer, we use  $Y$  for the vertical coordinate, with  $Y = 0$  defining the ground plane, i.e.,  $y/H = Y/H - 1$ .

Six different terrain conditions were used in Boundary Layer Wind Tunnel II at UWO, the properties of which are provided in Table 1. The high-speed test section for this wind tunnel has a length of 39m from the inlet to the centre of the turntable, a cross-section that is 3.4m wide and a nominal height of 2.4m at the location of the turntable. The six terrain conditions were made up of three different ground

roughness configurations, each of which was repeated with and without a 0.38m tall barrier at the test section inlet. As in Akon and Kopp (2016), the three terrain conditions with the barrier are labelled as 1L, 2L, and 3L, while the three without the barrier are 1S, 2S, and 3S. The number in these labels indicates the terrain roughness, while the label L indicates the presence of the barrier, which has a Larger integral scale, and the label S indicates that the no barrier was used, which results in a Smaller integral scale.

Figure 2 shows the vertical distributions of turbulence intensities for upstream conditions considered in this experiment measured at the location of the building model, but with the building removed. These boundary layers are identical to those reported by Akon & Kopp (2016) and Wu et al. (2017), where many further experimental details, including the mean velocity profiles, can be found. These are not repeated here due to length considerations, although it is noted that the mean velocity profiles normalized by the mean wind speed at the roof height are similar for  $Y/H < \sim 2$ . The turbulence intensities,  $I_u$ , and integral scales,  $L_x$ , range from  $I_u = 13\%$  with  $L_x/H = 6$  to  $I_u = 27\%$  with  $L_x/H = 12$ . Thus, there is a factor of two change in both intensity and scale in these data. Velocity spectra can be found in Wu *et al.* (2017). Further details of the experimental set-up can be found in Akon & Kopp (2016), Wu et al. (2017), and Akon (2017).

Table 1. Properties of the upstream boundary layer terrain conditions (from Akon & Kopp, 2016) and the maximum thickness of the mean separation bubble above the roof

| Terrain | Barrier height [m] | $I_u$ , at $y/H=0$ (%) | $L_x/H$ | $X_r/H$    | $T_b/H$ | $T_b/X_r$ |
|---------|--------------------|------------------------|---------|------------|---------|-----------|
| 1L      | 0.38               | 14                     | 13      | $\sim 1.4$ | 0.25    | 0.18      |
| 1S      | 0                  | 13                     | 6       | $\sim 1.4$ | 0.25    | 0.18      |
| 2L      | 0.38               | 17                     | 11      | 1.05       | 0.19    | 0.18      |
| 2S      | 0                  | 17                     | 8       | 1.05       | 0.21    | 0.20      |
| 3L      | 0.38               | 27                     | 12      | 0.88       | 0.17    | 0.19      |
| 3S      | 0                  | 26                     | 7       | 0.88       | 0.19    | 0.21      |

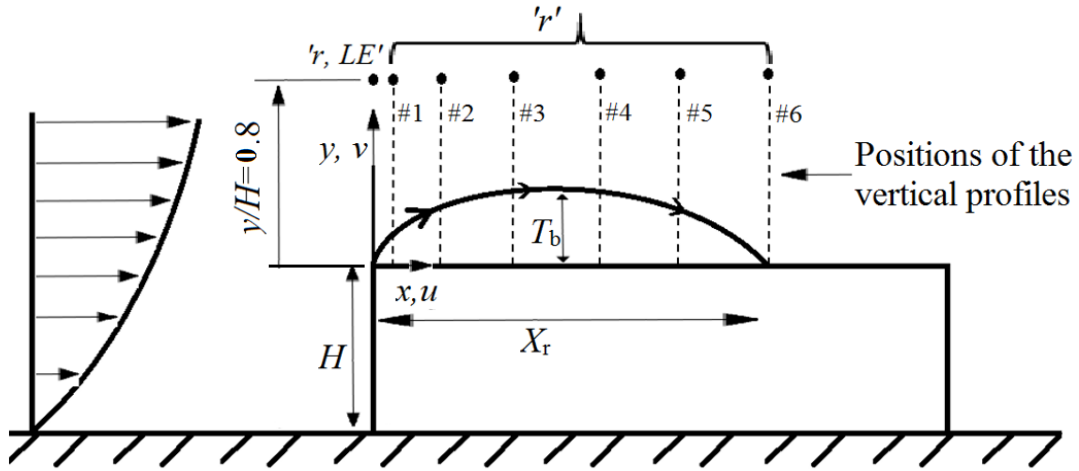


Figure 1. Schematic representation of the flow field, building set-up, and coordinate system. Detailed analysis positions are numbered, with precise locations provided in Table 2. The locations used for variable normalization are also provided.

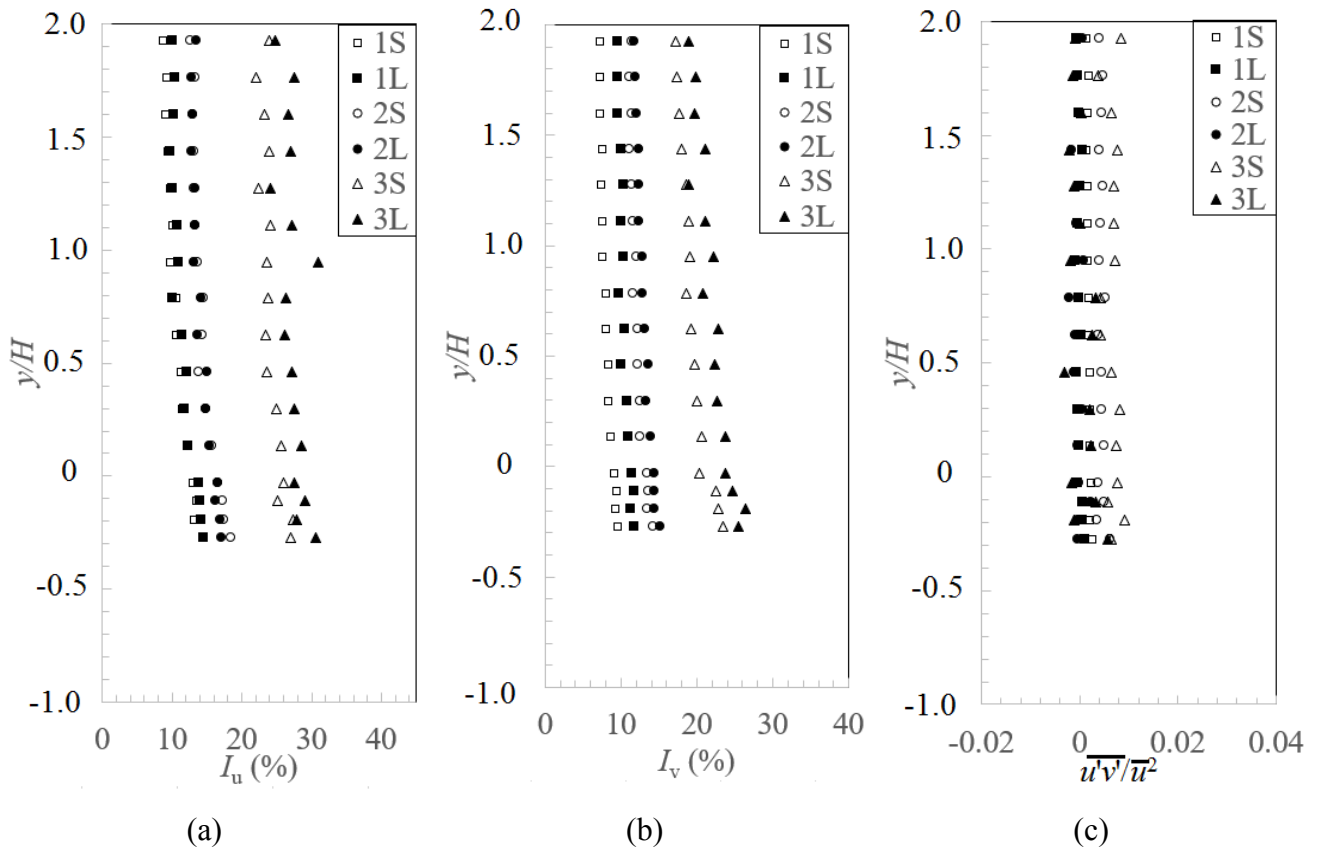


Figure 2. Vertical distributions of (a) streamwise turbulence intensity,  $I_u$ , (b) vertical turbulence intensity,  $I_v$ , and (c) Reynolds shear stress,  $-\frac{\overline{u'v'}}{(\overline{u})^2}$ , for the six terrain conditions. Note that  $y/H = 0$  is at the roof height, and  $y/H = -1$  is the ground plane.



In order to capture the velocity fields in and around the separation bubble on the roof surface, Time-Resolved Particle Image Velocimetry (TR-PIV) was used. Atomized olive oil was illuminated by a 22 mJ double-head, diode-pumped Q-switched Nd:YLF laser. PIV images were captured by two 1Mb Photron FASTCAM-1024 PCI CMOS cameras running in tandem at 1000 frames/s (i.e., sampling the velocity field at 500 Hz) for approximately 160 seconds. One of the cameras was used to capture the velocity field immediately upstream of the model and the other camera was used to capture the separated-reattaching flows over the roof centreline of the building model. A 20% overlap was maintained between the two fields of view. A time delay of 85 micro-seconds was used between the two images of a single image pair. A more detailed discussion on the TR-PIV system can be found in Taylor *et al.* (2010).

Utilizing an FFT cross-correlation algorithm, a commercial image processing software package, TSI Insight 4G, was used to calculate the velocity vectors. Interrogation windows of 32×32 pixels were used during processing the PIV raw images with 50% overlap. This resulted in a spatial resolution of the velocity field of 2 mm in both the streamwise and vertical directions. In the post-processing stage of the vector data, a global standard deviation filter, followed by local mean and median filters were used to find and replace bad vectors. Areas close to the model surfaces, where visible laser reflections were observed, were masked off and were discarded from analysis. The percentage of the bad vectors observed in the PIV fields of view was less than 5%. The spatial uncertainty of standard cross-correlation algorithms is approximately 0.1 pixels (Huang *et al.*, 1997). Wu *et al.* (2017) provide comparisons of the PIV measurements with four-hole Cobra pressure probe measurements (TFI, Inc. model no. 900) in the wind tunnel at the position of the building model, but with the building removed, that indicate good agreement between the two measurement systems.

### 3 Mean Velocity Field

In this section, the mean velocity field is investigated using various scaling parameters. Spatial distributions are examined via contour plots, line plots at various streamwise positions within the separation bubble, and by separation-streamline-based coordinates.

#### 3.1 Definitions of geometric scaling parameters

There are several parameters which could be used to examine the similarity of the mean and fluctuating flow fields for the different incident flow conditions, as discussed in the Introduction. For the vertical direction, these include: (i) the maximum thickness of the mean separation bubble,  $T_b$ , as defined in Figure 1, (ii) the building height,  $H$ , and (iii) the distance between the stagnation point on the windward wall and the roof edge,  $H_s$ . Akon & Kopp (2016) demonstrated that the location of the stagnation point did not depend on the upstream terrain conditions for a particular low-rise building, over the (realistic) range of terrain conditions that they considered. They found that  $H_s = 0.35H$ . Thus,  $H_s$  and  $H$  can be considered to be equivalent for purposes of similarity. The other vertical parameter is the maximum value of the mean distance of the SSL from the building surface,  $T_b$ , which can be viewed as a proxy for the shear layer thickness (a point which is examined in detail later in this section). In the horizontal direction, the main parameters would be (i) the mean reattachment length,  $X_r$ , and (ii) the length of the building,  $L$ . Since the current work is considering the flow above roofs of low-rise buildings, Kopp & Morrison (2018) have already established that the plan dimensions are not primary factors in controlling the roof pressure distributions, with building height being much more important. Thus, only  $X_r$  is considered here. The relationships between these parameters (i.e.,  $H_s$ ,  $H$ ,  $X_r$ ,  $T_b$ ) are also important since analysis of the flow would be simplified if they were to be related in fixed proportions.

Table 1 also provides the values of  $T_b/H$ ,  $X_r/H$ , and  $T_b/X_r$  for the six upstream conditions. The maximum thickness of the separation bubble,  $T_b$ , is determined by identifying the maximum vertical distance of the mean separating streamline from the roof surface. This streamline was, within the spatial resolution of the PIV measurements, the centre of the SSL, which is the point of maximum streamwise

velocity gradient. It should be noted that, due to the three-dimensionality of the flow, the streamline separating from the leading edge may not be the reattaching streamline. In fact, the authors attempted to identify the instantaneous reattachment points without success, such that the mean reattachment point is somewhat of an artifact. Nevertheless, the variable  $T_b$  is a reasonable measure of the maximum mean thickness of the separation bubble.

It is observed that a larger incident turbulence intensity causes both  $T_b$  and  $X_r$  to decrease. However, the values of  $T_b/X_r$  indicate that the ratio of these two parameters do not vary in the same way, with the higher turbulence intensities leading to relatively thicker separation bubbles, over the range considered. The integral scale also appears to affect this ratio, with a tendency to smaller  $T_b/X_r$  ratios for larger integral scales (although this is only observed for terrain conditions 2S/2L and 3S/3L, but not 1S/1L). Thus, the parameters that characterize the separated flow,  $T_b$  and  $X_r$ , do not have fixed relationships with each other or with parameters characterizing the building geometry,  $H$  (and  $H_s$ ). It can be concluded that separation bubbles are not geometrically similar and depend on the characteristics of the turbulence in the upstream terrain.

For much of this work, six different streamwise locations are used to examine vertical profiles of various flow parameters, such that each they are at the same values of  $x/X_r$ . In this normalization, the dimensional distance from the leading edge varies from one upstream condition to the other since the mean reattachment length depends on turbulence level, as shown in Table 1. In Figure 1, these non-dimensional locations are labelled as 1 – 6, with the actual values provided in Table 2.

In addition, the measured variables are normalized by parameters at vertical locations sufficiently far from the surface, such that the SSL does not influence these reference locations. These vertical locations are chosen to be  $y/H = 0.8$  above the roof (i.e.,  $Y/H = 1.8$ ), which will be shown later to be outside of the influence of the SSL. It should be emphasized that the fluctuations at these positions have relevance for surface pressures, as established by Wu & Kopp (2016) and Wu (2017). The properties of

the flow field at these reference points are denoted by the subscript ‘ $r$ ’ throughout the manuscript. Generally, there are insignificant variations of the normalizing parameters along the line  $y/H = 0.8$  for these reference positions, except where noted. Additionally, the subscript ‘ $r,LE$ ’, indicates a fixed reference location immediately above the leading edge, as shown in Figure 2.

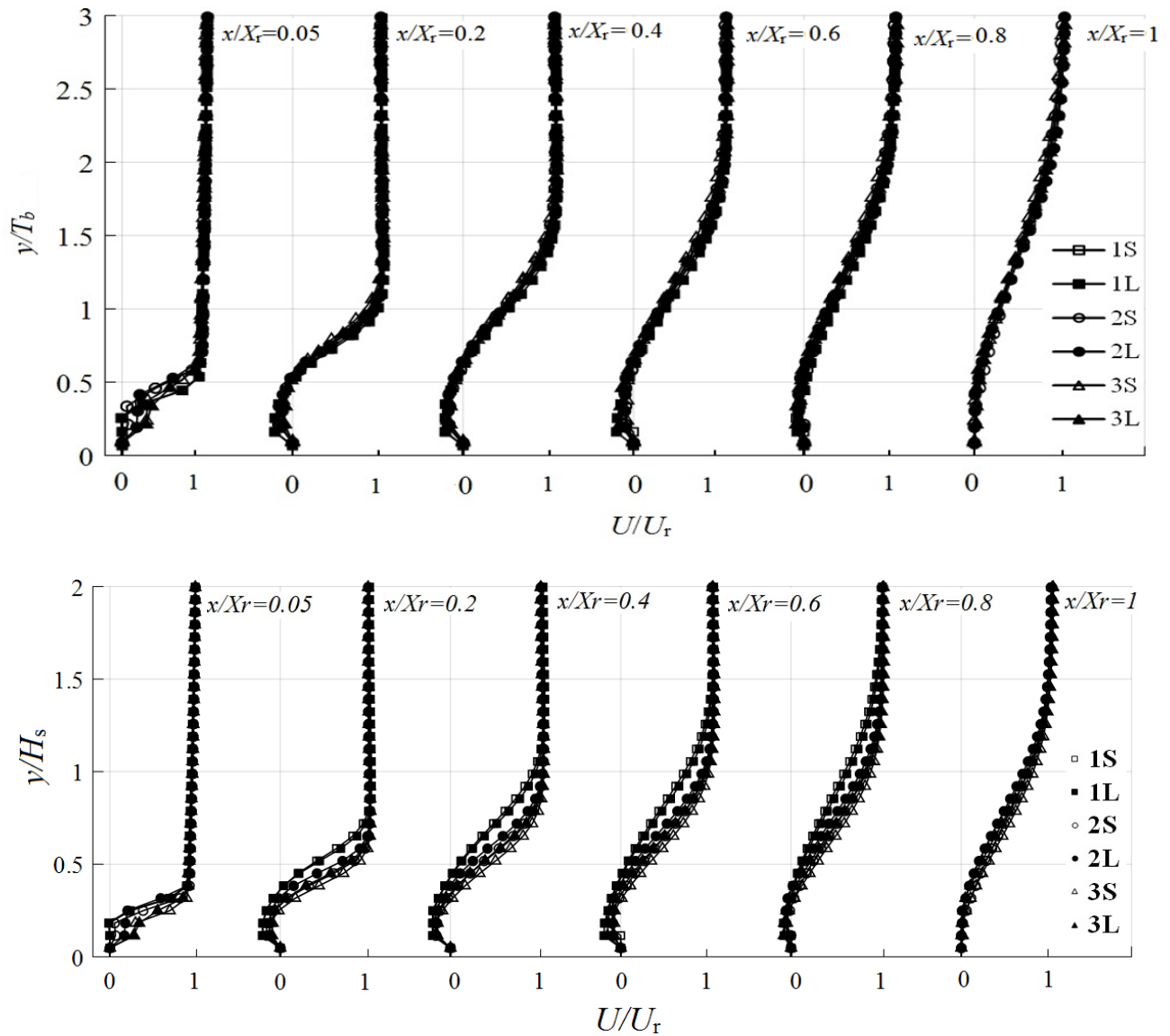


Figure 3. Vertical distributions of  $U/U_r$  as a function of position in the separation bubble normalized by (a)  $T_b$  and (b)  $H_s$ .

Table 2. Streamwise locations considered for flow variable profiles

| Location | 1    | 2   | 3   | 4   | 5   | 6   |
|----------|------|-----|-----|-----|-----|-----|
| $x/X_r$  | 0.05 | 0.2 | 0.4 | 0.6 | 0.8 | 1.0 |

### 3.2 Mean velocity profiles

Figure 3(a) shows the mean streamwise velocity,  $U$ , normalized by the local reference velocity,  $U_r$ . The vertical coordinate,  $y$ , is normalized by  $T_b$ , while each of the profiles is plotted at the  $x/X_r$  ratios provided in Table 2. It is observed that, irrespective of the turbulence intensity and length scales in the upstream terrain, the mean velocity profiles for the six cases are similar when normalized in this way, except in the early portions of the shear layer development, near  $x/X_r = 0.05$ . In contrast,  $H_s$  (and, therefore,  $H$ ) does not collapse the profiles, as can be seen in Figure 3(b). The separation bubble thickness,  $T_b$ , was also used by Castro & Haque (1987) to normalize the velocity field associated with the SSL of a blunt flat plate with a long splitter plate and  $I_u = 0.25\%$ . However, they only had a single configuration so the role of  $T_b$  in normalization could not be examined.

### 3.3 Vorticity thickness

To further examine the similarity of the mean flow field under different incident turbulence (i.e., terrain) conditions, the growth rates of the separated shear layers are examined. Growth rates of separated shear layers have typically been investigated via the vorticity thickness (e.g., Hancock, 2000; Agelinchaab & Tachie, 2008),

$$\delta_\omega = (U_{\max} - U_{\min}) / \left( \frac{\partial U}{\partial y} \right)_{\max} \quad (\text{Eq. 1})$$

However, for separated flows, the growth rates can also be investigated in terms of what has been called the maximum slope thickness (Cherry *et al.*, 1984), which is defined as,

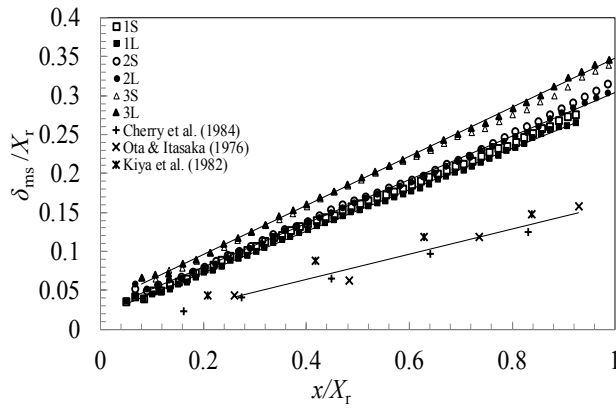
$$\delta_{\text{ms}} = U_{\max} / \left( \frac{\partial U}{\partial y} \right)_{\max} \quad (\text{Eq. 2})$$

The main difference between the two is how  $U_{\min}$  is treated within the separation bubble. Clearly, the values of  $U_{\min}$  are set to zero for the maximum slope thickness. Here we use both, in order to compare with different sets of previously published data.

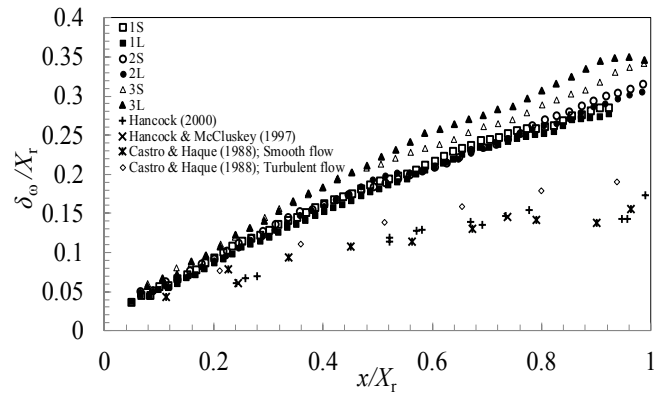
Figure 4(a) depicts the variation of  $\delta_{ms}/X_r$  for the six upstream conditions along with data from Cherry *et al.* (1984), Ota & Itasaka (1976) and Kiya *et al.* (1982) for two-dimensional bluff bodies placed in a uniform, smooth flow. In this figure, the mean reattachment length is used as the normalizing parameter. It is observed that the data from each experiment can be satisfactorily described by a linear relationship, similar to the case of the classical plane mixing layer. As reported by Brown & Roshko (1974), the growth rate of the plane mixing layer is in the range of  $\partial\delta_{ms}/\partial x \sim 0.14$  to  $0.22$ . It is noted that the slope does not depend on normalizing parameter when the same values are used in both the numerator and denominator. Evidently, SSL for two-dimensional bluff bodies in smooth flow have a similar growth rate ( $\sim 0.15$ ) as the classical plane mixing layer. The current data indicate that the addition of upstream turbulence increases the growth rate, with rates between  $0.26$  and  $0.32$  for  $I_u = 0.13$  and  $0.27$ , respectively. These higher growth rates in turbulent flow lead to maximum slope thicknesses that are substantially larger than those in the smooth stream.

Figure 4(b) shows the variations for the vorticity thickness,  $\delta_\omega/X_r$ , for the present experiments, along with the results of Hancock (2000) and Hancock & McCluskey (1997) for two-dimensional blunt flat plates with long splitter plates in uniform, smooth upstream flows, and Castro & Haque (1988) for both smooth and moderately turbulent flows ( $I_u = 3.0\%$ ). These data suggest that the growth of vorticity thickness along the SSL is not linear in smooth flow. This would appear to be related to the reversed flow near the surface within in the separation bubble, given the linear relationship found for the maximum slope thickness. This non-linearity is much less pronounced for the turbulent flow cases, again with much larger vorticity thicknesses for turbulent flow occurring in the latter half of the separation bubble.

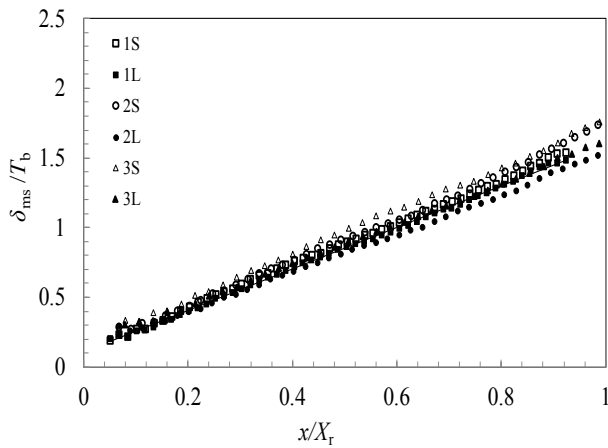
In Figures 4(a) and 4(b), where the thickness is normalized by  $X_r$ , it is observed that the results for the present experimental conditions do not collapse because of systematically higher growth rates in the latter portions of the separated shear layers for the cases with higher incident turbulence. Similar observations are made when these thickness parameters are normalized by  $H_s$  (not shown here). As discussed with respect to Figure 3, the separation bubble thickness,  $T_b$ , appears to be the more appropriate normalizing parameter for the mean velocity field. Figures 4(c)-(d) indicate that normalizing these thicknesses with  $T_b$  reduces the differences in the growth rate when compared Figures 4(a)-(b), although the data do not fully collapse.



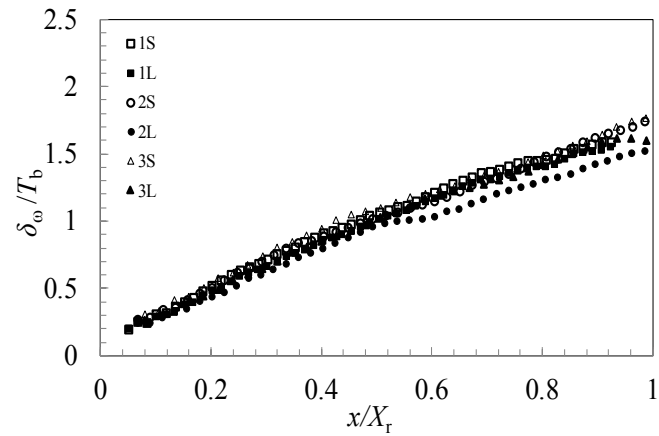
(a)



(b)



(c)



(d)

Figure 4. The growth of (a) maximum slope thickness,  $\delta_{ms}/X_r$ , (b) vorticity thickness,  $\delta_\omega/X_r$ , (c) maximum slope thickness,  $\delta_{ms}/T_b$  and (d) vorticity thickness,  $\delta_\omega/T_b$ .

### 3.4 Momentum thickness

Here, we consider the momentum thickness in shear layer coordinates, where  $s$  is the coordinate along the shear layer and  $y'$  is the coordinate normal to  $s$ . The momentum thickness is defined as,

$$\theta_T = \int_{LB}^{UB} \frac{U_s(y) - U_2}{U_1 - U_2} \left( 1 - \frac{U_s(y) - U_2}{U_1 - U_2} \right) dy' \quad (\text{Eq. 3})$$

where  $U_s(y')$  is the mean velocity at a point,  $y'$ , in the shear layer,  $U_1$  is the maximum mean velocity within the separated shear layer and  $U_2$  is the minimum mean velocity within the separated shear layer, all in the local shear layer coordinates  $(s, y')$ . The coordinate system used for this analysis,  $(s, y')$ , is sketched in Figure 5. The integration of  $\theta_T$  is conducted within the bounds defined by the shear layer turbulence, which are labeled as the lower (LB) and upper (UB) bounds. The shear layer turbulence is examined in the next section, but the definition of LB and UB are the points above the model roof surface where the changes in the turbulence kinetic energy are minimal, being 5% above the free stream values.

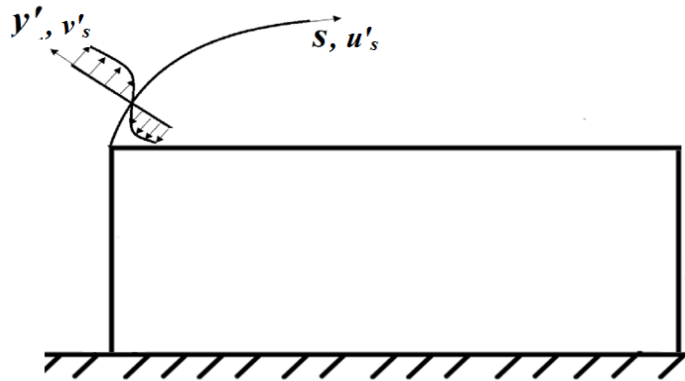


Figure 5. Schematic representation of the local shear layer coordinate system above the leading edge of the building.



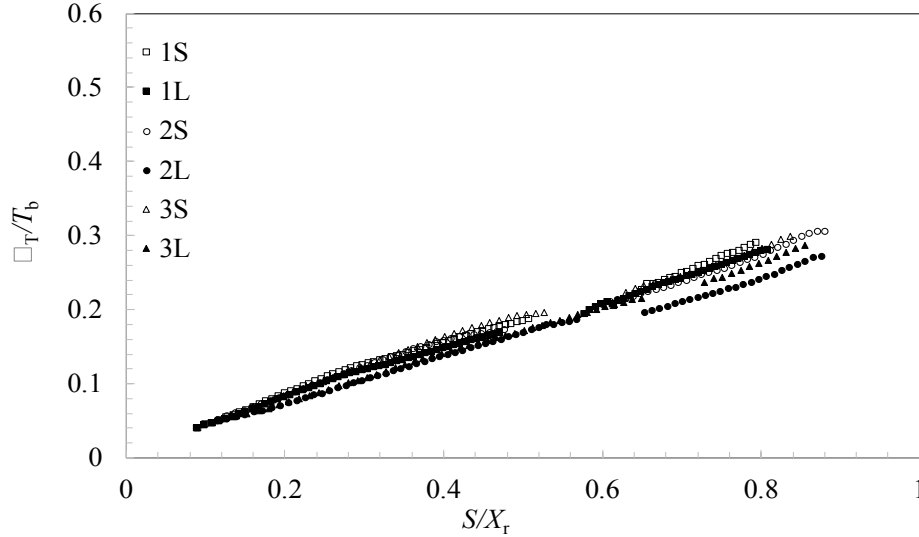


Figure 6. Momentum thickness,  $\theta_T$ , in local shear layer coordinates for the six terrain conditions.

Figure 6 shows the development of the momentum thickness along the separated shear layer, normalized by  $T_b$ . (It should be noted that “missing” data points in the plots result from the resolution of the vectors from the PIV data along certain lines, when translated into the streamline-based coordinate system.) It is observed that the growth of the momentum thickness along the separated shear layer is approximately linear for the current experiments, similar to the vorticity thickness, up to the mean reattachment point. Again, using  $T_b$  for normalization reduces the differences caused by the turbulence parameters to a great extent, although the collapse of data is far from perfect.

In summary: (i) The best scaling parameters for the mean separated-reattaching flow in highly turbulent incident flows are  $T_b$ , for the vertical direction, and  $X_r$ , for the streamwise direction; (ii) While the mean flow fields (i.e., the mean profiles and momentum thickness of the SSL) indicate approximate similarity using these parameters for the current range of terrain conditions, (iii) the shapes of the separation bubbles, as indicated by the  $T_b/X_r$  ratio, depend on both the scales and intensity of turbulence; (iv) The SSL are much thicker, growing at a faster rate than those placed in uniform, smooth incident flows or with relatively low levels of turbulence.

## 4 Turbulent Stresses

### 4.1 Streamwise Reynolds normal stress ( $\overline{u'u'}$ )

The contours of the Reynolds normal stress in the streamwise direction,  $\overline{u'u'}$ , normalized by the local reference values,  $\overline{(u'u')}_r$ , for upstream terrain conditions ‘1’ and ‘3’ are presented in Figure 7. With this normalization, the effects of turbulence in the SSL relative to the adjacent stream can be observed. On the contour plots, the mean streamlines are plotted along with the separating-reattaching streamlines, which are plotted as black lines in each figure. Overall, the contours have differences in both magnitude and shape. The mean streamlines are different for the terrains ‘1’ and ‘3’, reflecting the different reattachment lengths,  $X_r$ , which are most easily seen by identifying the centres of rotation in the separation bubbles and the SSL (black lines). As can be seen, the relative positioning of the regions with the highest values are different, with the contours for the rougher terrain (Figures 7(c)-(d)) occurring slightly further from the line denoting the SSL than for the smoother terrain (Figures 7(a)-(b)).

In terms of the magnitude of the streamwise velocity fluctuations plotted in Figure 7, it is clear that the relative magnitude of the contours in the SSL are higher for smoother terrains, when normalized by the adjacent stream levels (at the reference height,  $y/H = 0.8$ ). This is more clearly seen by the line plots in Figure 8, where the vertical profiles of  $\frac{\overline{u'u'}}{\overline{(u'u')}_r}$  are presented. Obviously, this type of normalization would be inappropriate for the case of a smooth stream, for which  $\frac{\overline{u'u'}}{\overline{(u'u')}_r} \rightarrow \infty$  with  $\overline{(u'u')}_r \approx 0$ . However, this type of normalization does indicate the relative levels of turbulence in the SSL compared to the adjacent stream, which is important for buildings in the atmospheric boundary layer. For all upstream conditions, it is observed that the heights of the maximum values in the profiles for each position do not collapse when normalized by either  $T_b$  (Figure 8) or  $H_s$  (not shown). As indicated by the contours in Figure 7, the location of the maximum occurs relatively further from the surface in the rougher terrain. Thus, there is

not similarity of the streamwise normal stresses within the SSL for the different terrain conditions in this normalization because of both the magnitudes and the spatial distributions.

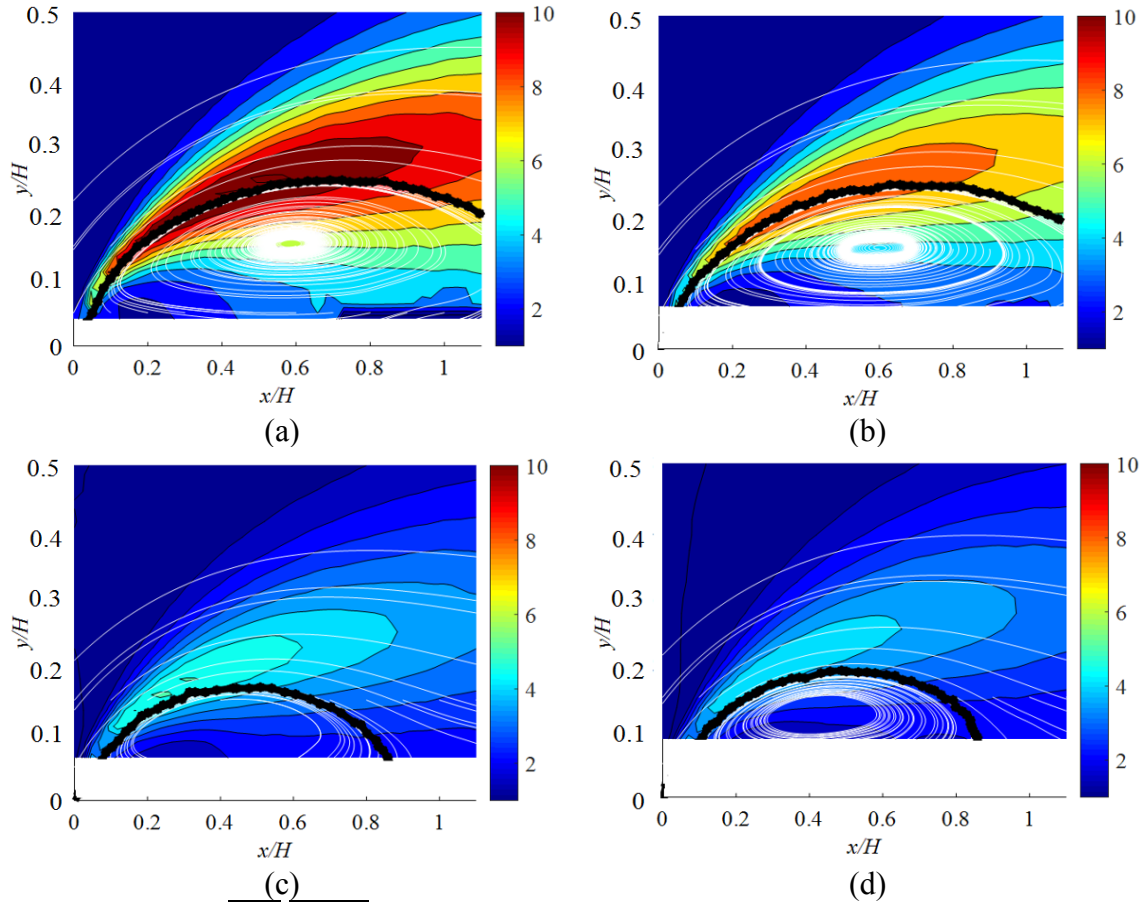


Figure 7. Contours of  $\overline{u'u'}/(\overline{u'u'})_r$  for upstream terrain conditions (a) 1S, (b) 1L, (c) 3S and (d) 3L.

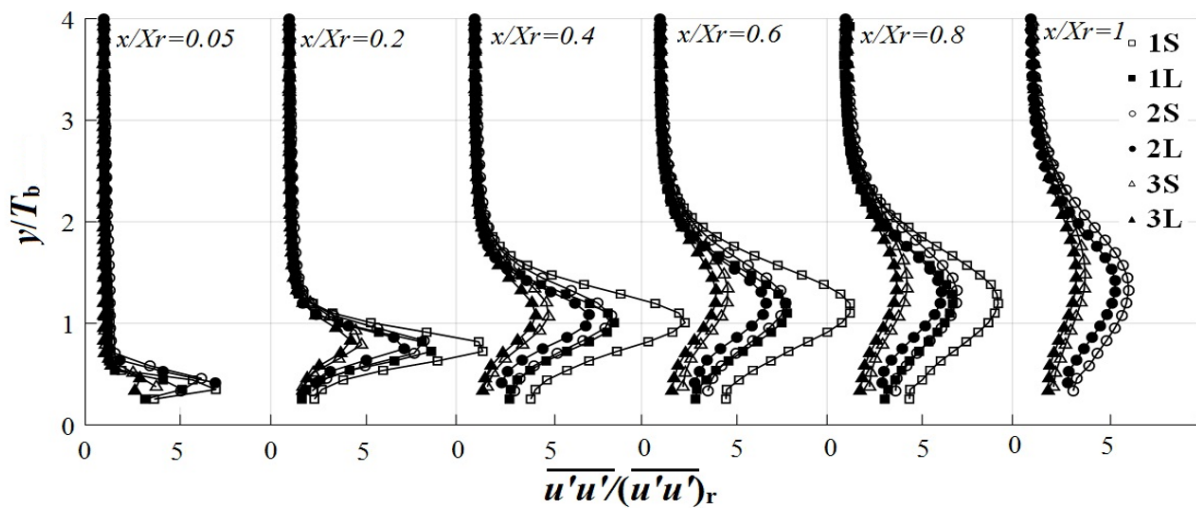


Figure 8. Vertical distributions of  $\overline{u'u'}/(\overline{u'u'})_r$ .

In Figure 9, the profiles of  $\overline{u'u'}$  are normalized by the square of the mean streamwise velocity at the reference height above the leading edge,  $U_{r,LE}^2$ . These plots, which contrast with those in Figure 8, represent the absolute differences in the magnitudes of  $\overline{u'u'}$  for the different terrain conditions. The plots reveal that the roughest upstream conditions, '3S' and '3L' (i.e., those with the highest turbulence levels), have the largest magnitudes at positions in and around the SSL. The maximum values increase up to about  $x/X_r \sim 0.2$  and then slowly decay for all terrain conditions.

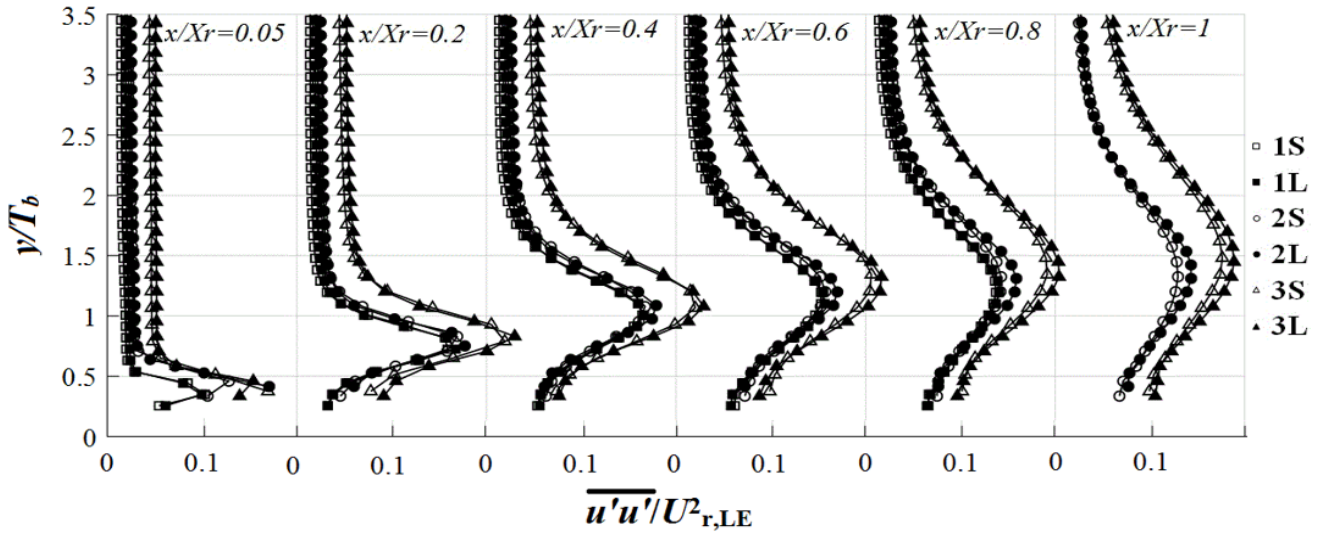


Figure 9. Vertical distributions of  $\overline{u'u'}/U_{r,LE}^2$ .

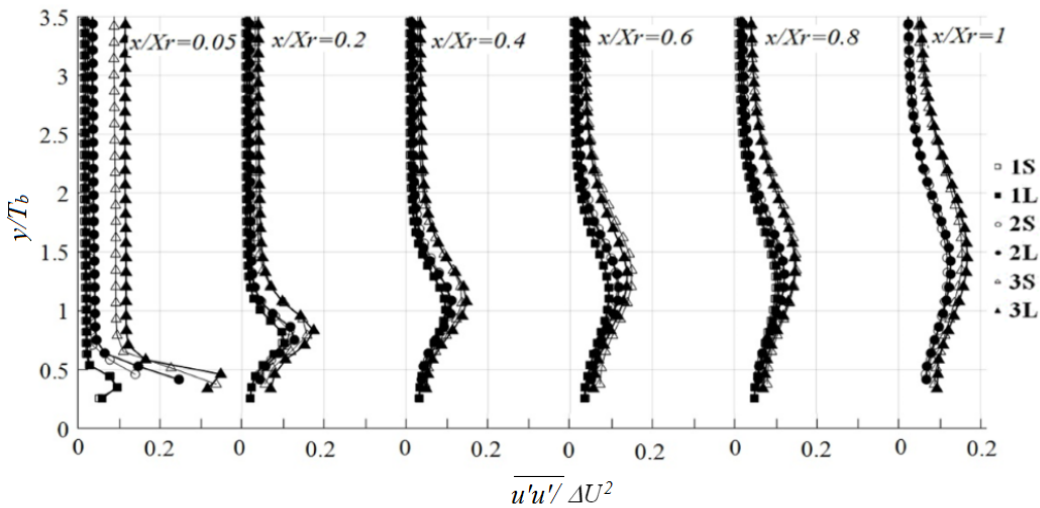


Figure 10. Vertical distributions of  $\overline{u'u'}/\Delta U^2$ .

To better understand the relative magnitudes of the turbulence in the SSL, Figure 10 depicts the profiles of  $\overline{u'u'}/\Delta U^2$ , where  $\Delta U = U_{max} - U_{min}$  is the maximum difference in the local mean velocities across the separated shear layer in the global  $x$ - $y$  coordinate system. (Note that  $\Delta U \neq U_1 - U_2$ , which is only used in the shear layer coordinate system shown in Figure 5.) The figure indicates that there are substantial differences in the relative values, with much higher levels when the upstream turbulence levels are higher, relative to the maximum mean velocity difference across the SSL. Thus, there is not a similarity of the profiles with respect to the upstream turbulence, which leads to different levels within the SSL. However, the use of the velocity difference across the shear layer,  $\Delta U$ , rather than just the fixed velocity at the leading edge,  $U_{r,LE}$ , reduces the differences between the data from the different terrains. Thus,  $\Delta U$  is a better normalizing parameter than  $U_{r,LE}$  within the SSL.

Figure 11 shows the variation of  $\overline{(u'u')}_{max}/\Delta U^2$  within the separation bubble, where two significant observations can be made regarding the effects of the upstream boundary layer turbulence. First, while the integral scale (over the range examined) appears to have minimal effects on these normal stresses, the upstream turbulence levels lead to distinct levels in the SSL with rougher terrains (i.e., higher upstream values) leading to relatively higher levels in the SSL. Second, the largest values of  $\overline{(u'u')}_{max}/\Delta U^2$  occur at the initiation of the SSL, which then decrease until about  $x/X_r > \sim 0.3$ , and then remain constant until about  $x/X_r \sim 1.0$ . This contrasts sharply with the results of Castro & Haque (1988), whose data indicate continuously growing levels of  $\overline{(u'u')}_{max}/\Delta U^2$ . In fact, they observe a more than doubling of values from  $x/X_r \sim 0.2$  to the point of mean reattachment, where the values are about 0.06 (see their Figure 9) for both cases (i.e., free stream turbulence levels of 0.25% and 3.0%). Thus, there are substantial differences in both the spatial development and the magnitudes of these Reynolds normal stresses in the current experiments on a low-rise building in the atmospheric boundary layer when compared to a normal flat plate with a long splitter plate in a flow with relatively low turbulence.

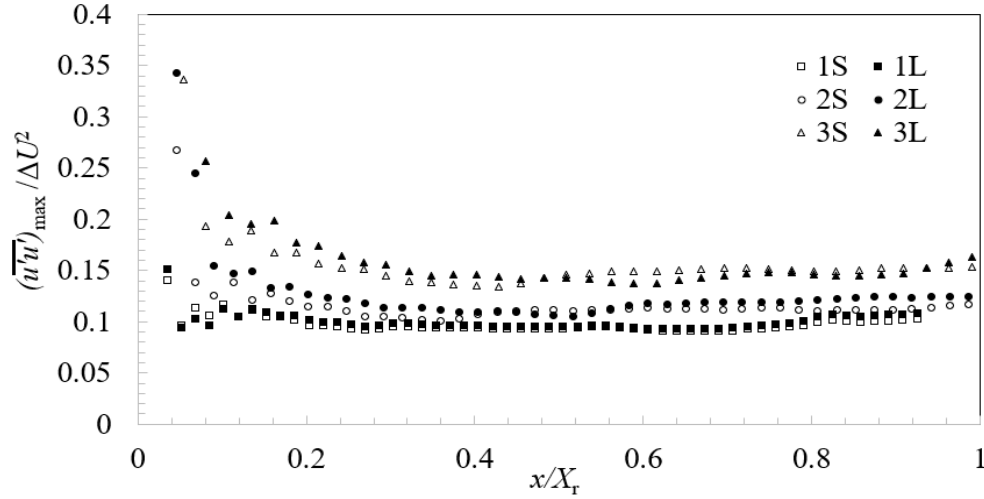


Figure 11. Variation of the maximum value of the Reynolds normal stress,  $(\overline{u'u'})_{max}/\Delta U^2$ , in the separated shear layers for the six terrain conditions.

## 4.2 Vertical Reynolds normal stress $(\overline{v'v'})$

The vertical profiles of  $\frac{\overline{v'v'}}{(\overline{v'v'})_r}$  (not shown), do not indicate similarity, with the highest relative values in the smoothest terrain, just like for the similar streamwise profiles. In contrast, the vertical profiles of  $\frac{\overline{v'v'}}{\Delta U^2}$ , shown in Figure 12, reveal that there are significant differences when compared to those for the streamwise values. In particular, the magnitudes of  $\frac{\overline{v'v'}}{\Delta U^2}$  at any axial location and for any upstream condition are never higher than 0.04. Comparing these results with the streamwise values reveals that the magnitudes of the vertical stresses are always significantly lower, since the maximum normalized values of the streamwise normal stresses are in the range from 0.10 to 0.16. Hence, the streamwise normal stresses are significantly larger than the vertical normal stresses and are the major contributor of the fluctuating flow field.

However, it is observed that, within the region of elevated vertical normal stresses associated with the SSL, the profiles have a greater tendency to be similar for  $x/X_r > \sim 0.4$ , with similar maximum values for each of the six terrain conditions. This indicates that the vertical Reynolds stresses within the SSL

become largely independent of the incident stream values as they grow in the magnitude for  $x/X_r > 0.2$ . The region of increasing magnitudes follows a region with initial decay for  $x/X_r < \sim 0.2$  where the values in the SSL depend on the upstream conditions. Thus, both the magnitudes and spatial distributions of the vertical normal stresses exhibit significantly differently behaviour than the streamwise normal stresses. These results are somewhat similar to those of Castro & Haque (1988), which indicate continuously growing values, but with values at  $x/X_r \sim 1.0$  of about 0.05 for  $I_u = 3\%$  and 0.065 for  $I_u = 0.25\%$ . Thus, one of the effects of the incident turbulence is to reduce the magnitude of this component.

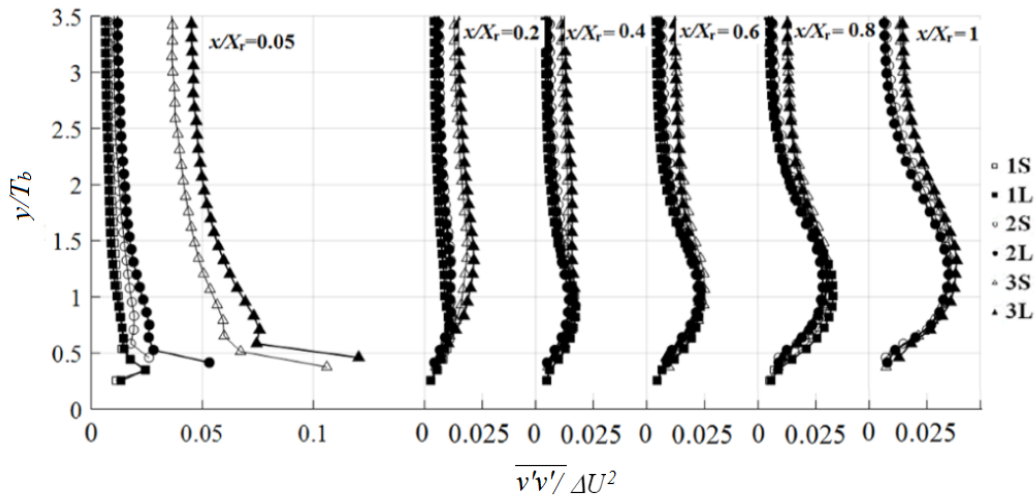


Figure 12. Vertical distributions of  $\overline{v'v'}/\Delta U^2$ .

### 4.3 Reynolds shear stress ( $-\overline{u'v'}$ )

The vertical distributions of  $-\frac{\overline{u'v'}}{\Delta U^2}$ , shown in Figure 13, indicate that the magnitudes of Reynolds shear stresses in the SSL vary between the six terrain conditions early in the development of the SSL, but are similar to each other for  $x/X_r > \sim 0.4$ . Thus, the effects of the varied boundary layer turbulence conditions are only observed in the initial development of the SSL, up to about  $x/X_r \sim 0.2$ . The largest magnitudes of  $-\frac{\overline{u'v'}}{\Delta U^2}$  are negative for  $x/X_r < \sim 0.2$  and positive for  $x/X_r > \sim 0.2$ . There is a sustained growth in maximum values of the normalized shear stresses,  $-\frac{\overline{u'v'}}{\Delta U^2}$ , for all x values, with initially negative

values near the separation point, a transition to positive values between  $x/X_r = 0.2$  and  $0.4$ , with increasingly positive values thereafter. As with the vertical normal stresses, it is observed that the maximum magnitudes of  $-\frac{\overline{uv}}{\Delta U^2}$  are significantly smaller than the maximum magnitudes of  $\frac{\overline{uu}}{\Delta U^2}$ , being about a factor of 3 to 5 smaller except close to the separation point.

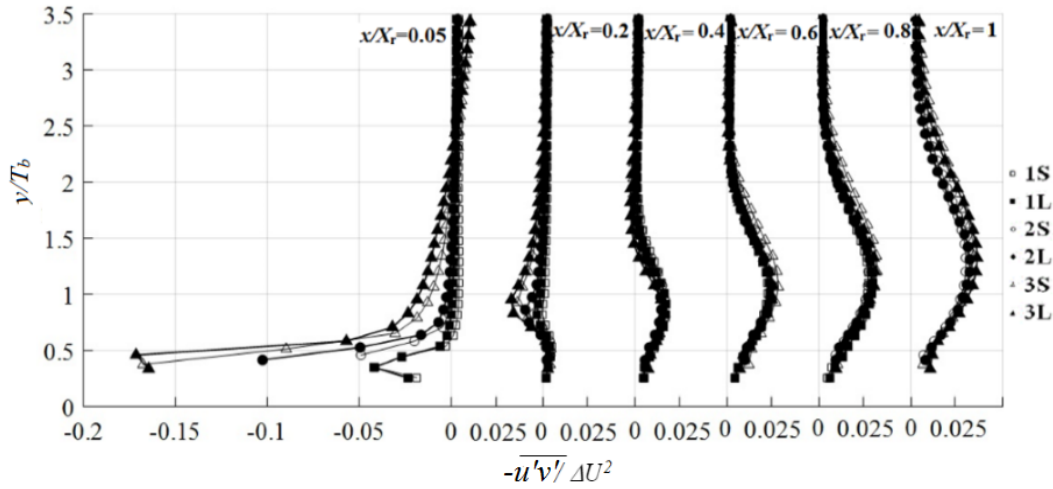


Figure 13. Vertical distributions of  $-\overline{u'v'}/\Delta U^2$ .

#### 4.4 Turbulence Structure

In summary, the normalized Reynolds normal and shear stresses depend on the upstream terrain conditions from the separation point at the windward edge up to about  $x/X_r \sim 0.4$ , with significant differences over this range for all six terrains. These differences have mostly disappeared for  $x/X_r > 0.4$  for  $\frac{\overline{vv}}{\Delta U^2}$  and  $-\frac{\overline{uv}}{\Delta U^2}$ , which indicates similarity of these stresses, for the terrain conditions studied, as they grow in magnitude beyond  $x/X_r > 0.4$ , to the mean reattachment point. In contrast,  $\frac{\overline{uu}}{\Delta U^2}$  does not indicate any sort similarity across the terrain conditions examined with different magnitudes and spatial distributions being maintained over the entire range of the separated flow. The streamwise normal stresses within the SSL are largest when the terrain conditions have the highest incident turbulence levels (in contrast to the vertical-normal and shear stresses). However, the normalized streamwise stresses are observed to decrease from the separation point until about  $x/X_r = 0.3$  to  $0.4$ , following which they remain



approximately constant. It is observed that  $T_b$  is the best scaling parameter for the vertical direction, while  $X_r$  is effective for the streamwise direction, noting that the ratio,  $T_b/X_r$ , depends on the upstream turbulence conditions. In addition, the maximum mean velocity difference across the SSL,  $\Delta U$ , is the most effective scaling parameter for the velocity field. Finally, over the range studied, the turbulence intensity is the more important parameter, with the integral scale having relatively less effect.

This general lack of flow similarity across terrains leads to mean pressure distributions in the separation bubble that depend on turbulence intensity. As observed by Akon and Kopp (2016), higher turbulence levels lead to relatively longer recovery distances for the surface pressures following separation. Wu *et al.* (2017) found that the “pressure recovery rates [in the separation bubble] are mainly due to increased turbulence-contributed pressure gradients near the roof surface” and that the “rate of recovery is not sufficiently high” to ensure a self-similar pressure distribution.

A second aspect caused by the lack of similarity across the terrains are differences in the turbulence structure, as indicated, for example, by  $(\overline{v_s'v_s'})/(\overline{u_s'u_s'})$ . Figure 14 depicts the ratios  $(\overline{v_s'v_s'})_{max}/(\overline{u_s'u_s'})_{max}$  for the six terrain conditions in the current study, along with values obtained from the Castro and Haque (1988) study. These data indicate that, for higher levels of turbulence in the incident stream, lower values of this ratio result. In the current study, as the separated shear layers approach the mean reattachment point, there are continuous increases in the vertical normal stress, while the streamwise normal stress remains approximately constant. This happens more rapidly for lower values of the incident turbulence such the  $(\overline{v_s'v_s'})_{max}/(\overline{u_s'u_s'})_{max}$  is 50% higher for terrains 1S/1L than for terrains 3S/3L by  $x/X_r = 0.75$ . For the lower turbulence cases of Castro & Haque (1988), both the vertical and streamwise normal stresses are observed to grow with downstream distance; however, the vertical stresses grow at a more rapid rate, leading to increasing values of the ratio as well. The vertical normal stresses are far higher in the SSL when there is lower turbulence in the incident stream.

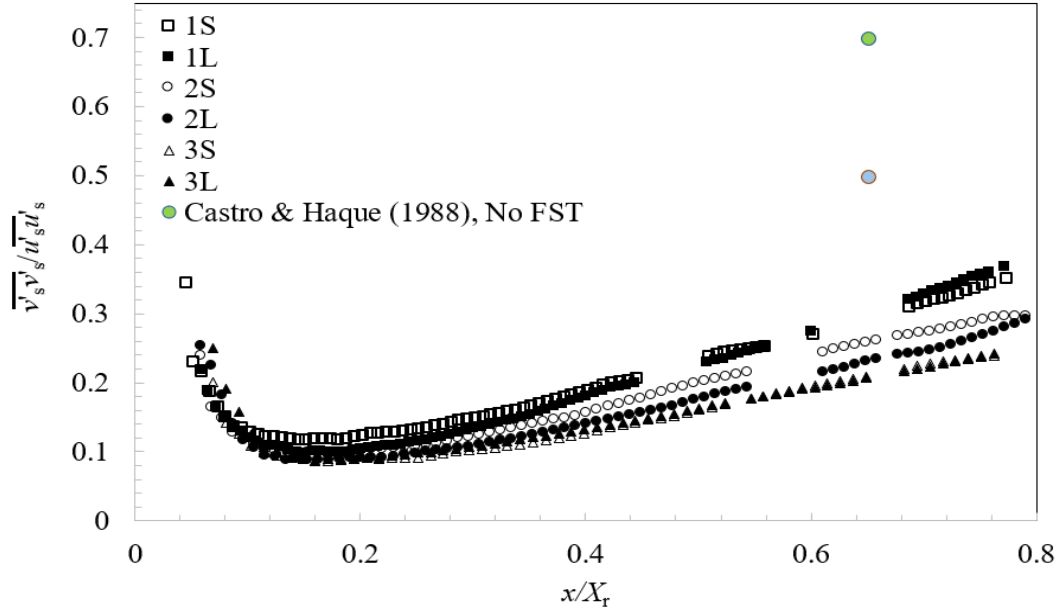


Figure 14. Distributions of  $\overline{(v'_s v'_s)}_{max} / \overline{(u'_s u'_s)}_{max}$  for the six terrain conditions, along with data from Castro and Haque (1988).

## 5 Normalized total turbulent kinetic energy ( $E_{kt}$ )

As originally proposed by Unal & Rockwell (1988), the normalized total turbulent kinetic energy across a separated shear layer is defined as

$$E_{kt} = \int_{LB}^{UB} \frac{k_t(y')}{\theta_T \Delta U_T} dy' \quad (\text{Eq. 4})$$

where  $\theta_T$  is the momentum thickness,  $\Delta U_T = U_1 - U_2$  is the maximum velocity deficit across the shear layer and  $k_t = (\sqrt{\overline{u'u'} + \overline{v'v'}})/2$ . Clearly,  $k_t^2$  is only an approximation of the turbulence kinetic energy since  $\overline{w'w'}$  was not be measured. However, this is a useful parameter for examining the flow structure.

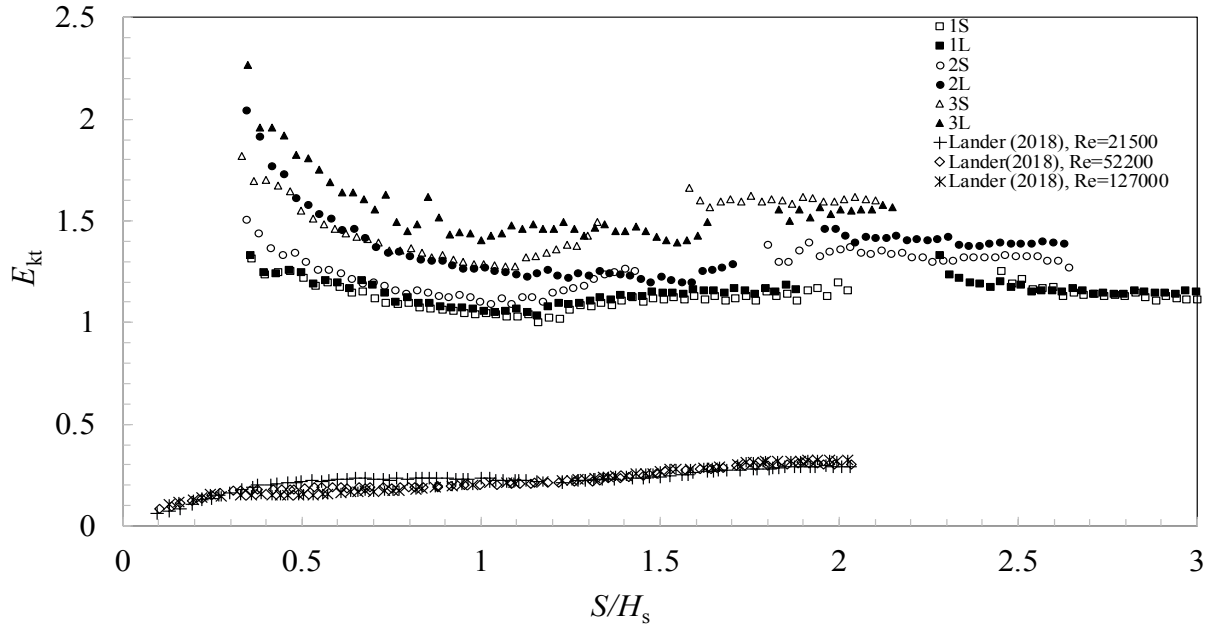
The integration is over the area of elevated turbulence associated with the SSL, as discussed earlier with respect to Eq. (3) for the momentum thickness. Lander (2017) suggests that  $E_{kt}$  can be used effectively to identify regions where there is growth in energy caused by Kelvin-Helmholtz instabilities, their eventual breakdown, and (in the case of their data) the rise of a secondary instability. PIV measurements by Lander (2017, 2018) of SSL generated by a two-dimensional square prism (i.e., a square cylinder)

reveal that  $E_{kt}$  grows linearly in regions that are associated with the formation of K-H vortices. The  $E_{kt}$  values then plateau in the region where the subsequent breakdown of vortices into full turbulence occurs. Thus, it is useful to examine the nature of the flow structure via this parameter, particularly with respect to the early regions of flow development, near the separation point. As can be inferred from the analysis of the previous section, the current data, obtained with the high turbulence levels characteristic of atmospheric boundary layers, change the development and levels of the Reynolds stresses and, therefore, the turbulence kinetic energy, when compared to those from smooth or low turbulence incident streams, although the early development of the turbulence parameter could not be examined in the Castro and Haque (1987, 1988) data.

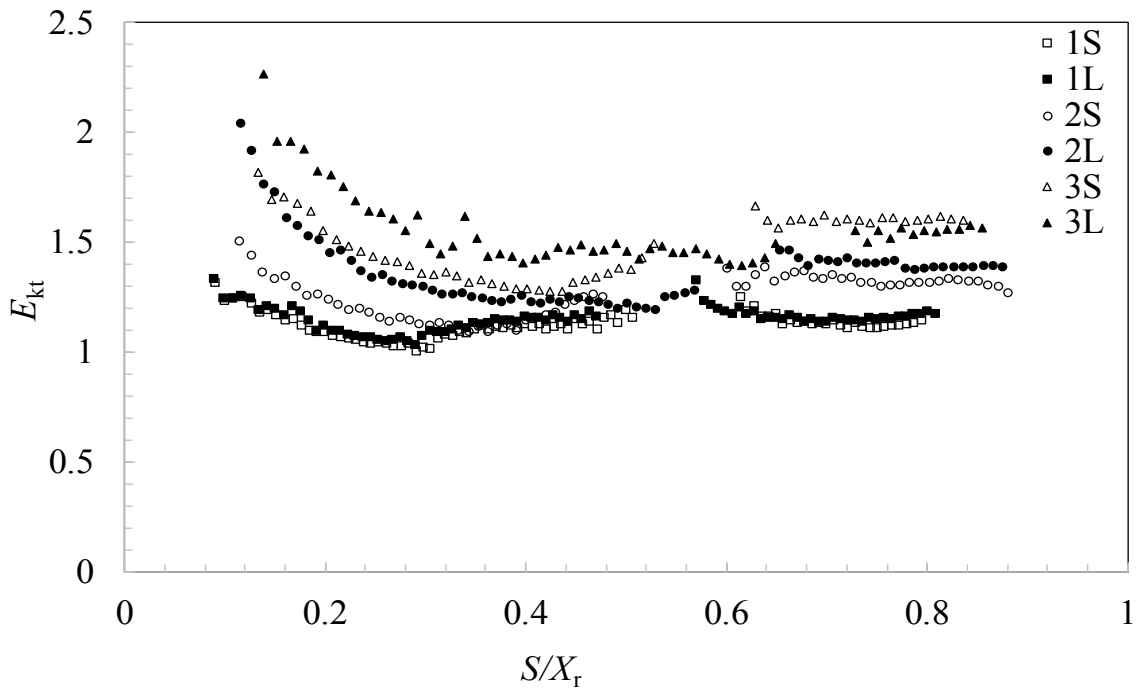
The measured distributions of  $E_{kt}$  along the shear layer, normalized by the height above the mean stagnation streamline,  $H_s$ , and the mean reattachment length,  $X_r$ , are presented in Figures 15(a)-(b), respectively. The use of  $H_s$  as a normalizing parameter in Figure 15(a) allows for direct comparison with the data of Lander (2018) for which there is no reattachment. The current data, for separated flow above the roof of a low-rise building, show significantly higher values of  $E_{kt}$ , compared to the results of Lander (2018). For the smooth flow case, the turbulent kinetic energy initially grows along the separated shear layer due to the formation of K-H vortices before plateauing. The pattern is significantly different in the current experiments, with an initial decrease in the normalized total turbulence kinetic energy before a plateau is reached. This suggests an initial decay of the turbulence, relative to the mean flow parameters, rather than a growth of vortices and the turbulence levels. In the current experiments, flows with higher levels of incident turbulence have both a greater initial decay rate and higher values of  $E_{kt}$  at the plateau. Both the integral scale and turbulence intensity affect these, although not uniformly, with variation caused by integral scales having similar effects as variations in the turbulence intensities. In all of the current experimental conditions, the decaying region occurs over a distance of up to about  $s/X_r \sim 0.3$  to 0.4, as can be seen in Figure 15(b). Further downstream the magnitude of  $E_{kt}$  remains basically constant

implying that a partial equilibrium has been reached in these flows such that the total turbulence kinetic energy is unchanging with respect to the momentum thickness and the mean velocity difference across the separated shear layer. Clearly, each SSL develops its own equilibrium state with different relative turbulence kinetic energy levels. However, this equilibrium is only partial, since the normal and shear stresses evolve at different rates, as shown in Section 4. Further, it is the streamwise normal stress which appears to control the lack of full similarity with respect to the terrain differences for  $x/X_r > \sim 0.3$ .

To examine this further, the instantaneous flow structure of the separated flow was examined, as done by Lander *et al.* (2016), and many others. As described by Chong *et al.* (1990), the second eigenvalue of the velocity gradient tensor,  $u_{ij} = \frac{\partial u_i}{\partial x_j}$  is an effective way of identifying vortices. The presence of complex eigenvalues of the velocity gradient tensor, for two-dimensional velocity fields, indicate the presence of a vortex (Taylor, 2011). Implementation of this method with PIV data was successfully done by Adrian *et al.* (2000) to identify vortices in a turbulent boundary layer and by Taylor *et al.* (2010) to identify the locations of the vortices around elongated bluff bodies. The positive complex portion of the eigenvalues of the velocity gradient tensor represent the strength of any local swirling motion (Zhou *et al.*, 1996, as described in Adrian *et al.*, 2000). This method is particularly useful to distinguish vortices in the flow where strong shear exists as the regions with high shear may show high values of vorticity without the presence of a real vortex in the region. Figure 16 shows a series of instantaneous contours of the swirling strength along with the simultaneous velocity vectors for terrain condition ‘1L’.

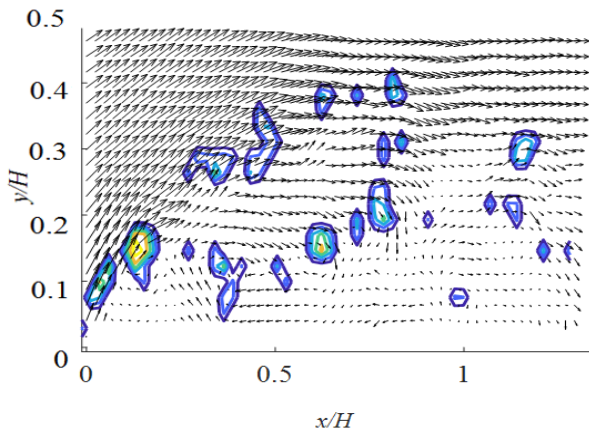


(a)

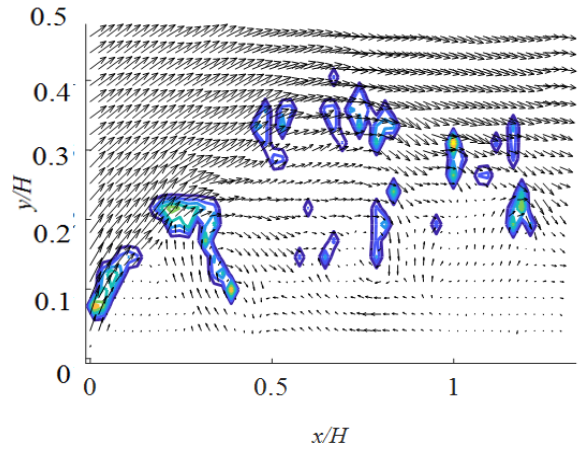


(b)

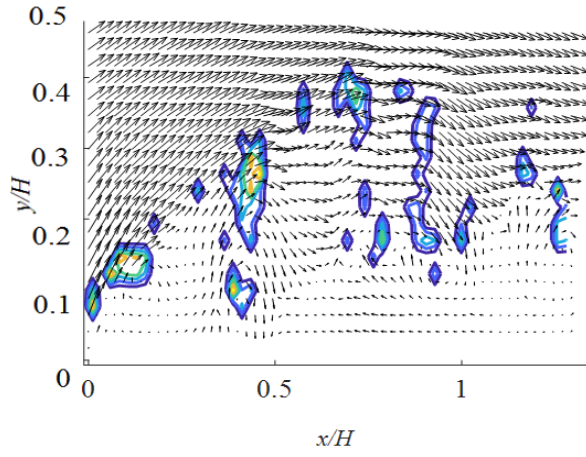
Figure 15. Distributions of the total turbulent kinetic energy,  $E_{kt}$ , along the separated shear layer as a function of (a)  $s/H_s$  and (b)  $s/X_r$ .



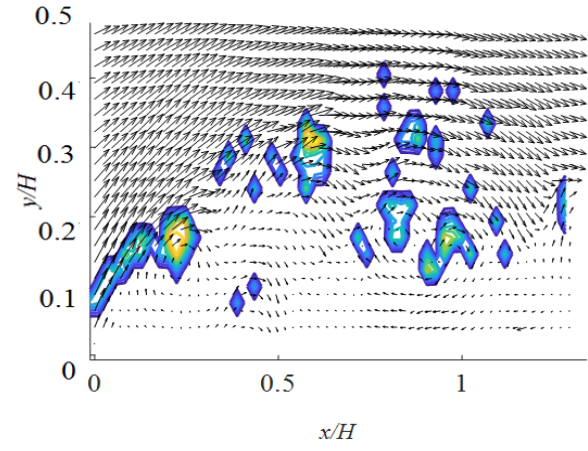
(a)



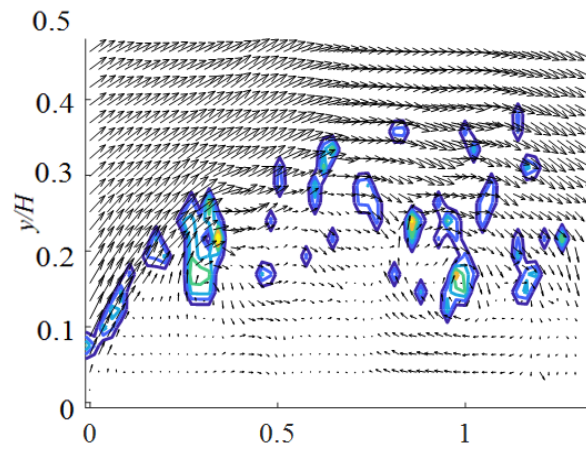
(b)



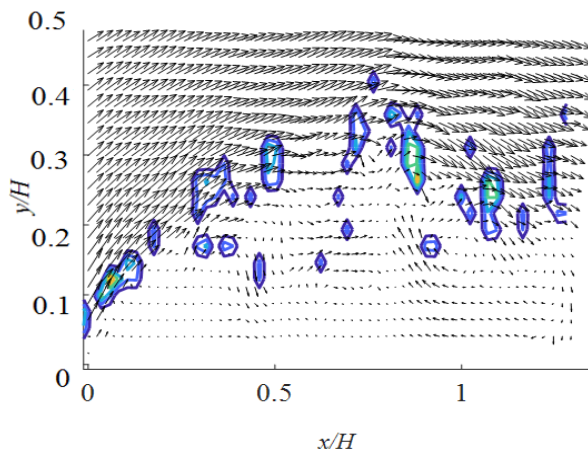
(c)



(d)



(e)



(f)

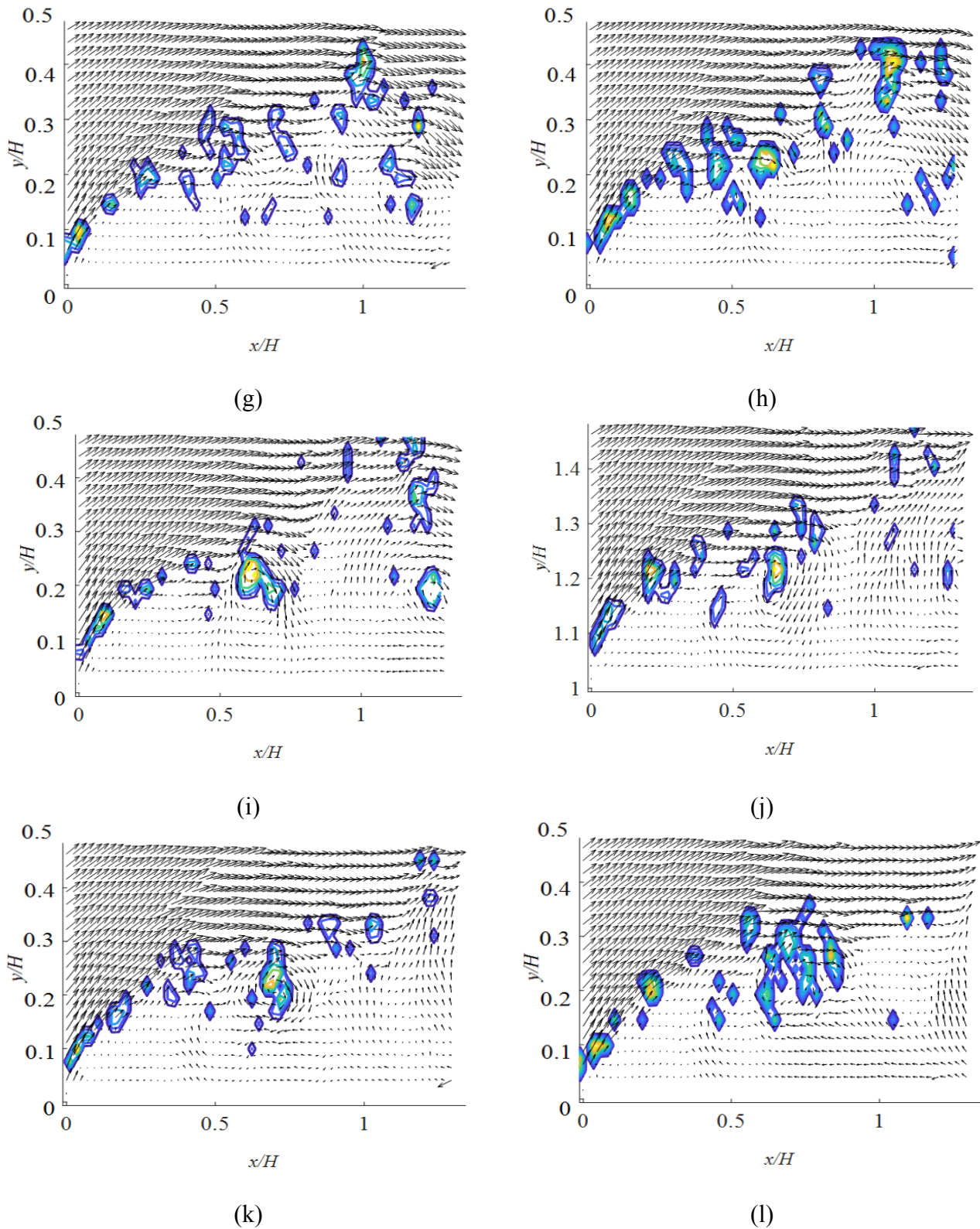


Figure 16. Typical sequence of instantaneous contours of swirling strength, superimposed on the simultaneous velocity field, for terrain simulation, 1L. Data were obtained at 500Hz, so each image is offset by 0.002s such that the total duration of the sequence is 0.022s.



Figure 16 indicates that there is a great deal of variability in the shear layer, with a range of vortex sizes, intensities, and distributions. The presence of vortices in the separated shear layer can be observed right from the separation point. However, there appears to be a general breakdown of the shear layer structure into turbulence at about  $x/H \sim 0.3$  to  $0.4$ , which is approximately the location where the normalized total turbulence kinetic energy becomes constant. At this point, the  $E_{kt}$  values indicate at least a partial equilibrium in the flow, as discussed above. This appears to be related to the breakdown of the initial vortices into turbulence.

The visual appearance of the separated shear layers in the initial formation region prior to the plateau is somewhat different from those presented in Lander *et al.* (2016, Figure 18), for both the smooth ( $I_u = 1.0\%$ ) and turbulent ( $I_u = 6.5\%$ ;  $L_x/H = 0.33$ ) incident flows. In the Lander *et al.* (2016) experiments, there is little indication of vortices at the initiation of the SSL, with K-H vortices emerging as the shear layer develops. In contrast, in the current study (Figure 16), the sizes of the initial vortical structures are substantially larger. The difference between the smooth flow results of Lander (2018), which indicate growth of turbulence kinetic energy as the K-H vortices are developing, and the current high turbulence cases (Figure 16 is for terrain '1L', with  $I_u = 14\%$  and  $L_x/H = 13$ ) in the present study, which show the initial decay in  $E_{kt}$  as the SSL develops, suggests that there may be a transition point between these two bounds. While Lander *et al.* (2016) did not examine the development of  $E_{kt}$ , their data indicate that pairing and growth in the SSL are still part of the process in a case with  $I_u = 6.5\%$  and  $L_x/H = 0.33$ . These authors suggest that there is a by-pass transition mechanism caused by small-scale turbulence on the stagnation streamline.

The current results suggest that there must be a state with sufficient levels of incident turbulence such that K-H stability cannot occur or that the process is altered in some significant way. In such a state, there is sufficient turbulence energy prior to the separation point such that larger-scale vortices exist (prior to separation), rather than forming as a result of the shear at the separation point. For incident



turbulence intensities above such a critical level, the effects of the incident turbulence on the development of the SSL are saturated in terms of their impact on the aerodynamic mechanisms: i.e., relatively large-scale vortices pass through the separation point, rather than being formed because of its existence. Then, for incident turbulence above the critical level, the shear layer vortices, which are relatively large compared to the momentum thickness of the SSL, decay following separation, instead of growing. However, the “signature” of incident turbulence remains, affecting the equilibrium value of  $E_{kt}$  in the SSL. For incident turbulence below the critical level, the turbulence structure is enhanced via the K-H instability (even with the by-pass transition), with  $E_{kt}$  increasing in magnitude following separation. Further work, via significantly higher resolution PIV measurements are required to better assess these mechanisms and to determine the critical values of turbulence intensity and scale where this saturation point occurs. With the relatively small initial decay in  $E_{kt}$  for the 1S/1L conditions, one suspects that it may be close to these values, at least for this size and geometry of building.

## 6 Conclusions

In this paper, the flow similarity of separated shear layers above the roof of a low-rise building is examined for six upstream terrain conditions with  $I_u$  varying from 13 to 27% and  $L_x/H$  varying from 6 to 13 at the roof height. The following conclusions can be drawn from the results and analysis:

- The mean reattachment length,  $X_r$ , is an appropriate scaling parameter along the streamwise direction for these separated-reattaching flows; however, neither  $X_r$ , nor building geometric parameters such as  $H_s$  or  $H$ , are appropriate for scaling the flow in the vertical direction. For the mean flow field, the maximum mean thickness of the separation bubble,  $T_b$ , is more appropriate.
- Separation bubbles on the roofs of low-rise buildings under these ABL turbulence conditions are not geometrically similar since the ratio of parameters defining the shape of the separation bubble,  $T_b/X_r$ , depends on both the turbulence intensity and scale.

- The non-dimensional Reynolds normal and shear stresses are not similar across these terrain variations. However, both the vertical normal and shear stresses are approximately similar for  $x/X_r > \sim 0.4$  up to the mean reattachment point, once the effects of incident turbulence are reduced. In contrast, the streamwise normal stresses do not exhibit similarity at all because they retain the characteristics of the incident turbulence across the entire domain of separated flow (and beyond).
- The total turbulence energy,  $E_{kt}$ , displays significantly different behaviour than that observed for separated flow in smooth incident flows. In smooth flow, other authors have observed that  $E_{kt}$  grows in magnitude from initiation at separation due to the Kelvin-Helmholtz instability and then plateaus during the vortex breakdown phase. In the current study, the initial turbulence levels are much higher, relative to the mean flow characteristics and there is an initial decay of  $E_{kt}$  followed by a plateau region. This suggests that the K-H instability is not active or is substantially altered in atmospheric boundary layer flows over low-rise buildings, at least for the range of conditions found in the current study. Future research should focus on identifying the turbulence intensities and scales for which such critical levels occur.

### **Acknowledgements**

This work was funded by the Natural Sciences and Engineering Research Council of Canada under the Discovery Grants program.

## 7 References

- Adrian, R. J., Christensen, K. and Liu, Z. 2000 Analysis and interpretation of instantaneous turbulent velocity fields. *Experiments in Fluids*. **29**, 275-290.
- Agelinchab, M. and Tachie, M. F. 2008 PIV study of a separated and reattached open channel flow over surface mounted blocks. *Journal of Fluids Engineering*. **130**, 061206- 1-9.
- Akon, A. F. 2017 Effects of turbulence on the separating-reattaching flow above surface-mounted, three-dimensional bluff bodies. *PhD thesis, University of Western Ontario, London, Ontario, Canada*.
- Akon, A. F, and Kopp, G. A., 2016 Mean pressure distributions and reattachment lengths for roof separation bubbles on low-rise buildings. *Journal of Wind Engineering and Industrial Aerodynamics*. **155**, 115-125.
- Brown, G. L. and Roshko, A. 1974 On density effects of large structures in turbulent mixing layers. *Journal of Fluid Mechanics*. **64**, 775-816.
- Castro, I. P. and Robins, A. G. 1977 The flow around a surface-mounted cube in uniform and turbulent streams. *Journal of Fluid Mechanics*. **79**, 301-335.
- Castro, I. P. and Haque, A. 1987 The structure of a turbulent shear layer bounding a separation region. *Journal of Fluid Mechanics*. **179**, 439-468.
- Castro, I. P. and Haque, A. 1988 The structure of a shear layer bounding a separation region. Part 2. Effects of free-stream turbulence. *Journal of Fluid Mechanics*. **192**, 577-595.
- Cherry, N. J., Hillier, R. and Latour, P. M. 1984 Unsteady measurements in a separated and reattaching flow. *Journal of Fluid Mechanics*. **144**, 13-46.
- Chong, M. S., Perry, A. E. and Cantwell, B. J. 1990 A general classification of three-dimensional flow fields. *Physics of Fluids*. **2 (5)**, 765-777.
- Essel, E. E., Nematollahi, A., Thacher, E. W. and Tachie, M. F. 2015 Effects of upstream roughness and Reynolds number on separated and reattached turbulent flow. *Journal of Turbulence*. **16**, 872-899.
- Fernandez-Caban, P.L. and Masters, F.J. 2018 Effects of freestream turbulence on the pressure acting on a low-rise building roof in the separated flow region. *Frontiers in Built Environment*. **4**,17. doi: 10.3389/fbuil.2018.00017.
- Gartshore, I. S. 1973 The effects of free stream turbulence on the grad of rectangular two-dimensional prisms. *University of Western Ontario*. BLWTL-4-73.
- Hancock, P. E. 2000 Low Reynolds number two-dimensional separated and reattaching turbulent shear flow. *Journal of Fluid Mechanics*. **410**, 101-122.
- Hancock, P. E. and McCluskey, F. M. 1997 Spanwise-invariant three-dimensional separated flow. *Journal of Experimental Thermal and Fluid Sciences*. **14**, 25-34.
- Huang, H., Dabiri, D. and Gharib, M. 1997 On errors of digital Particle Image Velocimetry. *Measurement Science and Technology*. **8**, 1427-1440.
- Kasagi, N. and Matsunaga, A. 1995 Three-dimensional particle-tracking velocimetry measurement of turbulence statistics and energy budget in a backward facing step. *International Journal of Heat and Fluid Flow*. **16**, 477-485.
- Kim, K. C., Ji, H. S. and Seong, S. H. 2003 Flow structure around a 3-D rectangular prism in a turbulent boundary layer. *Journal of Wind Engineering and Industrial Aerodynamics*. **91**, 653-669.
- Kiya, M. and Sasaki, K. 1983 Structure of a turbulent separation bubble. *Journal of Fluid Mechanics*. **137**, 83-113.
- Kiya, M. and Sasaki, K. 1985 Structure of large-scale vortices and unsteady reverse flow in the reattaching zone of a turbulent separation bubble. *Journal of Fluid Mechanics*. **154**, 463-491.
- Kiya, M., Sasaki, K. and Erie, M. 1982 Discrete vortex simulation of a turbulent separation bubble. *Journal of Fluid Mechanics*. **120**, 219-244.

- Kopp, G. A. and Morrison, M. J. 2018 Component and cladding wind loads for low-slope roofs on low-rise buildings. *Journal of Structural Engineering*. **144** (4), 04018019-1-11.
- Lander, D. C. 2017 Influence of freestream and forced disturbances on the shear layers of a square prism. *PhD thesis, Rensselaer Polytechnic Institute, Troy, New York, USA.*
- Lander, D.C. 2018 Personal Communication.
- Lander, D. C., Letchford, C. W., Amitay, M. and Kopp, G. A. 2016 Influence of the bluff body shear layer on the wake of a square prism in a turbulent flow. *Physical Review Fluids*. **1**, 044406- 1-28.
- Levitan, M. L., and Mehta, K. C., 1992 Texas Tech field experiments for wind loads part 1: building and pressure measuring system. *Journal of Wind Engineering and Industrial Aerodynamics*. **43** (1-3), 1565–1576.
- Lin, J. X., Surry, D. and Tieleman, H. W. 1995 The distribution of pressure near roof corners of flat roof low buildings. *Journal of Wind Engineering and Industrial Aerodynamics*. **56**, 235-265.
- Ota, T. and Itasaka, M. 1976 A separated and reattached flow on a blunt flat plate. *ASME Journal of Fluids Engineering*. **98**, 79-86.
- Saathoff, P. J. and Melbourne, W. H. 1997 Effects of free stream turbulence on surface pressure fluctuations in a separation bubble. *Journal of Fluid Mechanics*. **337**, 1-24.
- Taylor, Z. J., Gurka, R., Kopp, G. A. and Liberzon, A. 2010 Long-Duration Time-Resolved PIV to study unsteady aerodynamics. *IEEE Transactions on Instrumentation and Measurement*. **59**, 3262-3269.
- Taylor, Z. J. 2011 Vortex shedding from elongated bluff bodies. *PhD Thesis. University of Western Ontario, London, Ontario, Canada.*
- Unal, M. F. and Rockwell, D. 1984 The role of shear layer stability in vortex shedding from cylinders. *Physics of Fluids*. **27**, 2598.
- Wu, C-H. and Kopp, G. A. 2016 Estimation of wind-induced pressures on a low-rise building using Quasi-Steady theory. *Frontiers in Built Environment*. **2** (5).
- Wu, C-H., Akon, A. F. and Kopp, G. A. 2017 Effects of turbulence on the mean pressure field in the separated-reattaching flow above a low-rise building. *Journal of Wind Engineering and Industrial Aerodynamics*. **171**, 79-92.
- Wu, C-H 2017 Estimation of turbulence effects on wind-induced suction on the roof of a low-rise building. *PhD thesis, University of Western Ontario, London, Ontario, Canada.*
- Zhou, J., Adrian, R. J. and Balachandar, S. 1996 Auto-generation of near-wall vertical structures in channel flow. *Physics of Fluids*. **8**, 288-290.